Baroclinic Adjustment in an Atmosphere–Ocean Thermally Coupled Model: The Role of the Boundary Layer Processes

Citation: Zhang, Yang, and Peter H. Stone. "Baroclinic Adjustment in an Atmosphere–Ocean Thermally Coupled Model: The Role of the Boundary Layer Processes." Journal of the Atmospheric Sciences 68.11 (2011): 2710–2730. © 2011 American Meteorological Society

As Published: http://dx.doi.org/10.1175/jas-d-11-078.1

Publisher: American Meteorological Society

Persistent URL: http://hdl.handle.net/1721.1/73125

Version: Final published version: final published article, as it appeared in a journal, conference proceedings, or other formally published context

Baroclinic Adjustment in an Atmosphere–Ocean Thermally Coupled Model: The Role of the Boundary Layer Processes

YANG ZHANG

School of Atmospheric Sciences, Nanjing University, Nanjing, China

PETER H. STONE

EAPS, Massachusetts Institute of Technology, Cambridge, Massachusetts

(Manuscript received and in final form 1 March 2011)

ABSTRACT

Baroclinic eddy equilibration and the roles of different boundary layer processes in limiting the baroclinic adjustment are studied using an atmosphere–ocean thermally coupled model. Boundary layer processes not only affect the dynamical constraint of the midlatitude baroclinic eddy equilibration but also are important components in the underlying surface energy budget. The authors' study shows that baroclinic eddies, with the strong mixing of the surface air temperature, compete against the fast boundary layer thermal damping and enhance the meridional variation of surface sensible heat flux, acting to reduce the meridional gradient of the surface temperature. Nevertheless, the requirement of the surface energy balance indicates that strong surface baroclinicity is always maintained in response to the meridionally varying solar radiation. With the strong surface baroclinicity and the boundary layer processes, the homogenized potential vorticity (PV) suggested in the baroclinic adjustment are never observed near the surface or in the boundary layer.

Although different boundary layer processes affect baroclinic eddy equilibration differently with more dynamical feedbacks and time scales included in the coupled system, their influence in limiting the PV homogenization is more uniform compared with the previous uncoupled runs. The boundary layer PV structure is more determined by the strength of the boundary layer damping than the surface baroclinicity. Stronger boundary layer processes always prevent the lower-level PV homogenization more efficiently. Above the boundary layer, a relatively robust PV structure with homogenized PV around 600–800 hPa is obtained in all of the simulations. The detailed mechanisms through which different boundary layer processes affect the equilibration of the coupled system are discussed in this study.

1. Introduction

One basic issue in studying the midlatitude general circulation is to understand and quantify the relation between baroclinic eddies and the mean flow. For this purpose, several theories have been proposed, including one that focuses on the baroclinic adjustment. The baroclinic adjustment theory, which was first introduced by Stone (1978) and further studied by Gutowski (1985), Cehelsky and Tung (1991), Lindzen (1993), Welch and Tung (1998), Zurita and Lindzen (2001), and Zurita-Gotor and Lindzen (2004a,b), proposes a preferred equilibrium state of the mean flow with relatively robust isentropic slope/potential vorticity (PV) structure and a tendency of baroclinic eddies to homogenize the mean flow PV. However, when comparing this theory with observations, as shown in Stone and Nemet (1996) and Kirk-Davidoff and Lindzen (2000), the baroclinic adjustment is found only in the free troposphere with homogenized PV observed around 600–800 hPa, and it fails to work in the boundary layer. The observed strong surface baroclinicity at midlatitudes challenges the validity of the baroclinic adjustment.

On the other hand, many studies indicate that boundary layer processes have a strong influence on the development and equilibration of baroclinic eddies. Linear baroclinic instability studies showed that the Ekman friction leads to a reduction in instability (Card and Barcilon 1982; Lin and Pierrehumbert 1988), and the thermal damping, as shown by Valdes and Hoskins

Corresponding author address: Yang Zhang, 22 Hankou Road, Nanjing, Jiangsu 210093, China.
E-mail: yangzh@alum.mit.edu

DOI: 10.1175/JAS-D-11-078.1

(1988), has small influence on the instability, which may destabilize the flow under some circumstance. Nonlinear eddy life cycle studies by Branscome et al. (1989) and Gutowski et al. (1989) found that surface momentum and heat fluxes all act to suppress the maximum amplitude that baroclinic eddies can reach in the life cycle. Eddy equilibration studies indicate that different boundary layer processes may have different mechanisms that influence the baroclinic eddy equilibration and the equilibrated state. Swanson and Pierrehumbert (1997) suggested that surface heat flux and the boundary layer vertical thermal diffusion damp the surface air temperature fluctuation on very short time scales and may prevent the temperature mixing by baroclinic eddies. Surface friction may affect the eddy equilibration through more complex ways. The mechanism of ''barotropic effect'' (James and Gray 1986; James 1987; Chen et al. 2007) indicates that surface friction can affect the baroclinic eddy equilibration by modifying the horizontal shear of the zonal flow. Zurita and Lindzen (2001) noted that short Charney waves can equilibrate by mixing the PV gradient only around the critical level. Zurita-Gotor and Lindzen (2004b) thus suggest that surface friction, by affecting the zonal wind, can change the distribution of the critical level, which also affects the baroclinic eddy equilibration and limits the PV homogenization.

Zhang et al. (2009, hereafter Z09), under the lower boundary condition of fixed SST, studied how these boundary layer processes work together to influence the baroclinic equilibration and limit the PV homogenization. Z09 showed that the boundary layer vertical thermal diffusion and surface heat exchange are the dominant processes that prevent the boundary layer PV homogenization. These two processes couple the boundary layer, even the free troposphere, with the underlying surface and strongly damp the lower-level temperature fluctuations. Thus, even though the potential temperature mixing by the baroclinic eddies in the boundary layer is strong, the strong surface temperature gradient is still retained. Z09 also found that reducing surface friction alone does not result in efficient elimination of the boundary layer PV gradient and the response of the equilibrated state PV gradient to changes in surface friction is not monotonic. These results are obtained under the condition of fixed surface temperature; thus, through the boundary layer processes, the lower surface behaves as a permanent source of the lower atmosphere baroclinicity. This is a reasonable assumption as long as the atmospheric adjustment time scale is short compared with the underlying surface temperature variation time scale. However, for the longer time scale climate dynamics, fixed surface temperature is a considerable limitation. Whether the mechanism suggested in Z09 works in longer time scales may depend on whether the strong surface temperature gradient can still be maintained in spite of the strong surface air mixing by baroclinic eddies. Many studies also suggested that coupling between the atmosphere and ocean reduces the surface thermal damping (Bladé 1997; Barsugli and Battisti 1998; Ferreira et al. 2001) compared with the uncoupled run, which also indicates that the role of the boundary layer processes in limiting the PV homogenization needs further investigation in the coupled system.

The boundary layer processes, especially the surface heat fluxes, not only affect the dynamical constraint of the baroclinic eddy equilibration in the extratropics, but also are important components in the underlying surface energy budget (da Silva et al. 1994; Kållberg et al. 2005). The surface heat fluxes not only affect the eddy activity in the atmosphere directly but also strongly contribute to the variation of the underlying surface temperature (Frankignoul 1985; Stull 1988), which in turn affects the baroclinic eddy equilibration in the atmosphere. Thus, the surface energy balance, through the boundary layer processes, is an important factor that constrains the atmospheric eddy equilibration, which is always neglected in the previous studies. In this study, we release the condition of fixed surface temperature in Z09 and further investigate the baroclinic adjustment and the role of the boundary layer processes in a simple atmosphere–surface thermally coupled model. As the baroclinic adjustment is based on the quasigeostrophic (QG) concept, the atmospheric model used here is still a QG process model, as in Z09. The underlying surface chosen in this study is a slab ocean. How the atmospheric eddy activity, boundary layer processes, and the surface energy balance work together to determine the equilibration of the coupled system is the topic we will investigate here. More specifically, compared with the fixed SST situation, what is the role of the different boundary layer processes in limiting PV homogenization as well as the baroclinic adjustment? These are the questions that we will answer in this study.

Our study illustrates the dominant role of baroclinic eddies in determining the surface sensible heat flux distribution, which acts to reduce the surface baroclinicity. Nevertheless, in all the cases, under the requirement of surface energy balance, strong surface baroclinicity is always maintained in response to the meridional variation of the incident solar radiation. Combined with the boundary layer processes, the PV homogenization is always suppressed in the boundary layer. The detailed mechanisms by which different boundary layer processes affect the equilibration of the coupled system by modifying the eddy activity and the surface energy budget are investigated. Compared with the uncoupled runs in Z09,

boundary layer processes limit the PV homogenization as well as the baroclinic adjustment in a more uniform way—that is, the PV homogenization is more efficiently suppressed under stronger boundary layer damping no matter how the surface baroclinicity is modified. Above the boundary layer, a robust PV structure with homogenized PV around 600–800 hPa, as suggested by Zurita and Lindzen (2001) and Zurita-Gotor and Lindzen (2004a), is obtained.

The structure of this paper is assigned as follows. Section 2 is a brief description of the atmosphere–ocean thermally coupled model. The spinup of the coupled model and the effect of the lower-level eddy mixing in modifying the underlying surface temperature distribution are shown in section 3. The roles and mechanisms of different boundary layer processes in limiting the PV homogenization in the coupled runs are investigated in section 4. A summary and discussion of the results are presented in section 5.

2. Model description

The atmospheric model used in this study is still a modified β-plane multilevel quasigeostrophic channel model with interactive static stability and a simplified parameterization of atmospheric boundary layer physics, similar to that of Solomon and Stone (2001a,b) and Z09. The model has a channel length of 21 040 km, which is comparable to the length of the latitudinal belt in the midlatitudes, and a channel width of 10 000 km with the baroclinic zone over the central half of the channel. For simplicity the radiative–convective forcing in the atmosphere is still parameterized by the Newtonian cooling form. One difference between the coupled and uncoupled models is that the radiative–convective equilibrium (RCE) state temperature T_e used in the radiative–convective forcing, instead of being fixed, is allowed to vary with the underlying surface temperature T_g in the coupled model. Thus, the variation of the surface temperature can be "felt" by the atmosphere through the boundary layer processes and the radiative–convective heating. Here we only introduce the boundary layer parameters used in the model. As in Z09, four coefficients c_{dt}, c_{df}, μ_s, and μ_m are used to parameterize the strength of the surface sensible heat exchange, surface friction, boundary layer thermal and momentum diffusions, respectively. In addition, surface friction by ageostrophic winds is also included in most of the simulations. (See appendix A for the details of the atmospheric model.)

A slab ocean model is coupled with the atmospheric model to provide an interactive distribution of T_g. The slab ocean model has a fixed depth and only allows heat exchanges with the atmosphere (i.e., surface sensible and latent heat fluxes and radiative flux) to influence the surface temperature directly. In the model, the dynamical heat transport in the ocean (i.e., oceanic meridional heat transport) is simply represented by a prespecified Q flux $Q_{\rm fx}$, which is not allowed to vary with time. Since this study focuses on midlatitude dynamics, sea ice is not included in the model, even though snow and ice have a strong influence on the albedo, static stability, and poleward heat transport in high latitudes.

a. Governing equation of the surface temperature

The tendency of T_g is calculated from the energy budget equation of the surface layer:

$$\rho_g C_{pg} H_{\rm sur} \frac{\partial T_g}{\partial t} = F_{\rm sur} + Q_{\rm fx}, \tag{1}$$

where ρ_g is the seawater density of the ocean mixed layer and is constant in the model; C_{pg} is the specific heat and $\rho_g C_{pg}$ is 4×10^6 J m^{-3} K^{-1} for ocean surface; $H_{\rm sur}$ is the depth of the surface layer; $F_{\rm sur}$ is the heat flux across the air–sea interface (define the flux from the atmosphere into the surface as positive); and $Q_{\rm fx}$ represents the effect of the convergence of oceanic horizontal heat transport and the possible heat flow into the ocean mixed layer from deeper layers. Even though the depth of the ocean mixed layer has large spatial and seasonal variation, for simplicity we assume $H_{\rm sur}$ to be a constant with $H_{\rm sur} = 5$ m as the default value in this study. In the midlatitudes, the ocean mixed layer is typically around 100 m in the winter and 20 m in the summer. However, the equilibrium state of the coupled system is insensitive to $H_{\rm sur}$. Even for the transient response, we found the surface response time scale with a shallow ocean mixed layer is already much longer than the atmospheric response time scales, and the mechanism through which the coupled system reaches the equilibrium is the same.

Note that $F_{\rm sur}$ has three components: radiative flux into the surface $F_{\rm rad}$; sensible heat flux from the surface to the atmosphere $F_{\rm sh}$, which has the same definition as in Eq. (A4); and latent heat flux from the surface to the atmosphere $F_{\rm lh}$:

$$F_{\rm sur} = F_{\rm rad} - F_{\rm sh} - F_{\rm lh}. \tag{2}$$

Our atmospheric model is a dry model that does not simulate moist physics. The net thermal forcing of radiative and latent heating is parameterized in a Newtonian cooling form. However, these two factors are important terms in the surface energy budget and estimated explicitly in the surface model.

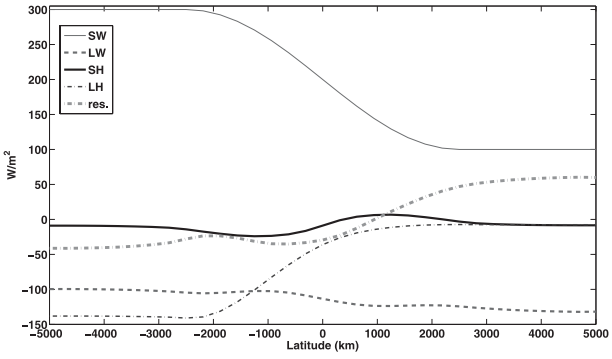

FIG. 1. Latitudinal distribution of the specified shortwave radiation, the estimated longwave radiative flux, sensible and latent heat fluxes from the calibrated state atmospheric and surface temperature, and the Q flux estimated as the residual value to maintain the calibrated state surface energy balance.

b. Latent heat flux

The latent heat flux is estimated using the linear bulk aerodynamic formula:

$$F_{\rm lh} = c_{dl}\rho_s L(q_g - q_{\rm air}), \tag{3}$$

where L is the latent heat of evaporation and c_{dl} is the drag coefficient of latent heat flux; $c_{dl} = B_o c_{dt}$ is proportional to the drag coefficient of sensible heat. The ratio between the two drag coefficients B_o, whose physical meaning is analogous to the Bowen ratio, is a constant in the model. Thus, varying c_{dt} in our model will result in changes in both sensible and latent heat fluxes at the surface. We assume that the mixing ratio of water vapor at the surface q_g is equal to the saturation mixing ratio q_g^* at the temperature of the surface. The actual water vapor mixing ratio of the surface air $q_{\rm air}$ is expressed in terms of the relative humidity (RH), with $q_{\rm air} = {\rm RH} \times q_{\rm air}^*$. In this model, we assume that RH = 0.8.

c. Radiative flux

The net radiative flux $F_{\rm rad}$ has two components: net solar radiation (SW) and net longwave radiation (LW). In our model, SW is specified, as shown in Fig. 1, varying from 100 to 300 W m^{-2} over the central half of the channel.

Note that ${\rm LW} = F_{\rm lw}^{\downarrow} - F_{\rm lw}^{\uparrow}$. The upward longwave radiation from the surface into the atmosphere $F_{\rm lw}^{\uparrow} = \epsilon_g \sigma T_g^4$, where $\epsilon_g = 0.95$ is the emissivity of the surface and σ is the Stefan–Boltzmann constant. The downward longwave radiation into the surface $F_{\rm lw}^{\downarrow}$ is estimated from a simplified radiative transfer equation:

$$F_{\rm lw}^{\downarrow}(\tau_g) = \int_0^{\tau_g} -\sigma T^4(\tau')[e^{(\tau'-\tau_g)/\mu_1} + e^{(\tau'-\tau_g)/\mu_2}]\, d\tau', \tag{4}$$

where τ_g is the optical depth at surface. Detailed definitions of each variable, as well as the derivation of Eq. (4), are supplied in appendix B.

d. Q flux

To obtain a surface temperature distribution similar to the current climate, a Q flux is included in the surface model. For the ocean surface, the Q flux represents the effect of the meridional ocean heat transport and the heat exchange between the mixed layer and the deep ocean. The Q flux is precalculated from the surface energy budget using climatological surface temperatures, an algorithm suggested by Russell et al. (1985) and Hansen et al. (1988).

To estimate the Q flux, a calibration run is carried out with a 43-K surface temperature difference over the central half of the channel as the calibrated state, which is also the observed temperature difference over the Northern Hemisphere midlatitude during winter. In the calibration run, the surface temperature is specified with the calibrated state distribution and kept fixed. Only the atmospheric model is integrated until it reaches an equilibrium state. With the equilibrium state air temperature and the specified surface temperature, the sensible and latent heat fluxes and longwave radiative flux are calculated from Eqs. (A4), (3), and (4), respectively. Their meridional distributions are displayed in Fig. 1. Under the specified solar radiation, the Q flux is estimated as the residual of the surface energy budget from Eq. (1). As shown in Fig. 1, the magnitudes of these fluxes and their meridional variation over the channel are comparable to the observations (Hsiung 1986; da Silva et al. 1994; Trenberth and Caron 2001). Our surface model can capture the features of the meridional variation of the surface energy fluxes reasonably well.

3. Spinup of the coupled model

To show the roles of baroclinic eddies and Q flux in maintaining the equilibrium of the coupled system, the coupled model is spun up in three steps. The latitudinal distributions of surface temperature in the equilibrium state in these steps are plotted in Fig. 2a.

1) Without Q flux and turning off the zonal variation of the coupled system (without eddies), we integrated the 2D symmetric model for 3000 days. In the equilibrium state, as shown in Fig. 2a (which is the state averaged over the last 1000 days), a steep meridional surface temperature gradient appears across the channel with the north–south temperature contrast as large as 75 K.
2) Starting from the equilibrium state of the symmetric run, we run a 3D simulation with small-amplitude perturbations in zonal wavenumbers 1–10 added at

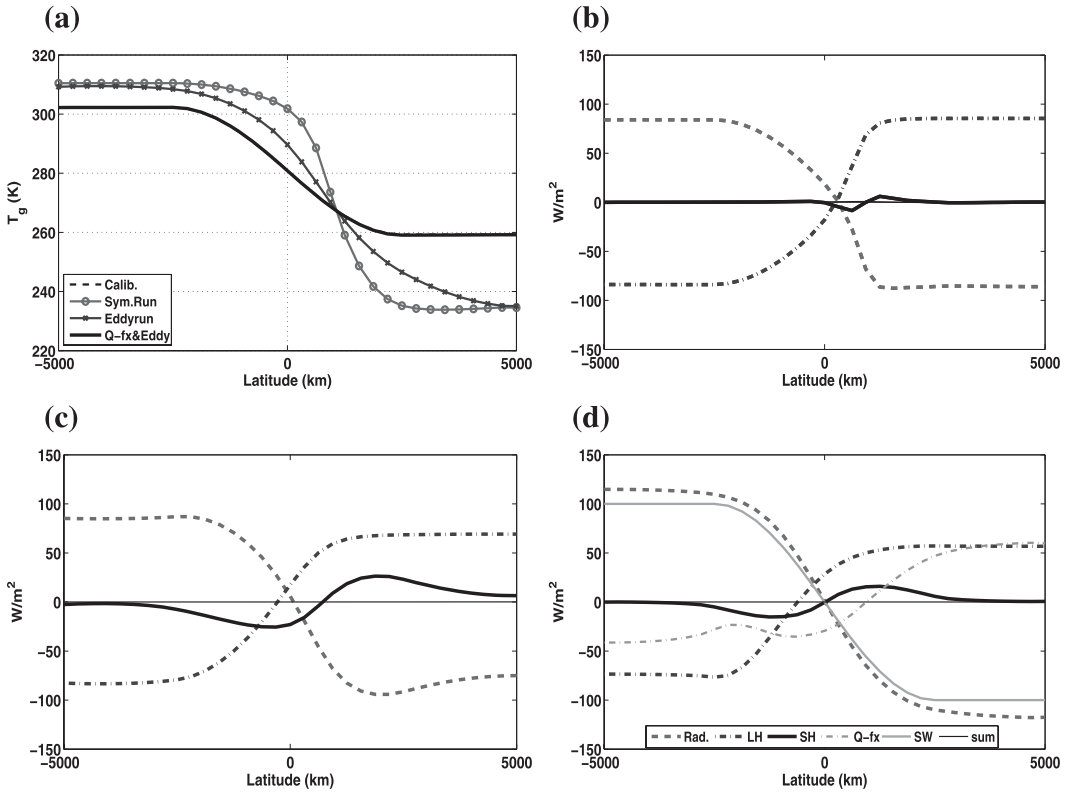

FIG. 2. (a) Latitudinal distribution of the equilibrium state surface temperature for the three runs compared with the calibrated state temperature, and (b)–(d) the radiative flux, latent heat flux, and sensible heat flux anomalies (deviation from the horizontal mean) in the surface heat budget for (b) the 2D run, (c) the 3D run without Q flux, and (d) the SD run. The latitudinal variance of the shortwave radiation into the surface (solid gray) is also plotted in (d).

the initial moment. Because of the strong baroclinicity of the mean flow, baroclinic eddies quickly spin up in the atmosphere. After hundreds of days, the coupled system reaches an equilibrium state, as shown in Fig. 2a, with the temperature gradient near the center of the channel greatly reduced.

3) Then we run the 3D simulation including the Q flux. In equilibrium, the surface temperature gradient is further reduced. A 43-K meridional temperature difference of the underlying surface is obtained, which is also the calibrated state as well as the observed wintertime temperature difference across the midlatitudes of the Northern Hemisphere. This 3D simulation with the Q flux is also taken as the standard (SD) run in the following studies.

Latitudinal variations of each energy flux in the surface energy budget in the 2D and 3D runs without Q flux and in the SD run are plotted in Figs. 2b–d, respectively. As we mainly focus on the baroclinicity of the equilibrium state, only the deviation (anomaly) of each flux from its horizontal mean is plotted, through which the variation of surface energy flux in these steps is better illustrated. The horizontal average of each field shows little variation in these steps (results not shown here), which is almost the same as in Fig. 1. In Fig. 2d, meridional variation of the specified solar radiation into the surface is also plotted; its difference from the total radiative flux also shows the distribution of the longwave radiation.

The surface energy budget shows strong variations in these runs. Without baroclinic eddies, as shown in Fig. 2b, the meridional variation of sensible heat flux is almost negligible. Latent heat flux, with steep meridional variation, is the dominant component to balance the radiative flux. When turning on baroclinic eddies, sensible heat flux, despite having a smaller magnitude than latent heat flux, makes a greater contribution and helps to balance the radiative forcing. The meridional variation of the latent heat flux in equilibrium becomes smoother. In the SD run, as shown in Fig. 2d, meridional variation of the latent heat flux is further reduced and becomes comparable with the Q flux. They are the two major components that balance the solar radiation in the surface energy budget. Sensible heat flux makes a smaller contribution in the SD run. The longwave radiation, which is the difference between the net radiation and the solar radiation, shows minor

meridional variations. Compared with Fig. 1, the meridional variation of each energy flux is almost the same as in the calibration run, which can simulate the distribution of each surface energy flux reasonably well. Thus, from the comparison of the surface energy budget in these runs, we find that (a) the existence of baroclinic eddies enhances the meridional variation of the sensible heat flux, which acts to reduce the meridional variation of the surface temperature; (b) even though the sensible heat flux can adjust the meridional surface temperature distribution, the energy balance of the underlying surface is still primarily maintained by the latent heat flux and the radiative flux (more specifically, shortwave radiative flux); and (c) with the Q flux, the meridional variation of surface temperature is strongly reduced and the meridional variation of the solar radiation is balanced by the latent heat flux and Q flux.

The different variations of the sensible and latent heat fluxes in the spinup runs come from their different dependence on the surface and air temperature as well as the eddy activity. The sensible heat flux, as indicated in Eq. (A4), is primarily determined by the air–sea temperature difference and the drag coefficient. The surface heat exchange always acts to reduce the air–sea temperature difference. In the 2D run, the surface sensible heat flux is the only dominant process that determines the surface air temperature, which acts on the surface air within a very quick time scale. The surface air temperature, thus, is forced to be almost equal to the underlying surface. Baroclinic eddy mixing of the surface air temperature is another factor that determines the air–sea temperature difference. When baroclinic eddies are included, the meridional eddy heat transport will result in cold surface air anomalies in the lower latitudes and warm surface air anomalies in the higher latitudes. Thus, baroclinic eddies, by mixing the surface air temperature, can enhance the sensible heat flux and result in a weaker surface temperature gradient as shown in Fig. 2a. Furthermore, we would expect that stronger eddy mixing of the surface air temperature can result in stronger air–sea temperature differences as well as greater sensible heat flux. This is consistent with a comparison of Figs 2c and 2d. With the stronger baroclinicity as well as stronger eddy activity (results not shown here), a stronger meridional variation of the sensible heat flux is observed compared with the SD run and obvious sensible heat flux into the ocean is even obtained at higher latitudes.

The latent heat flux, from Eq. (3), can be expanded as

$$F_{\mathrm{lh}} = c_{dl} L \rho_s (q_g^* - \mathrm{RH} q_{\mathrm{air}}^*) \approx c_{dl} L \rho_s [(1 - \mathrm{RH}) q^*(T_g) - \mathrm{RH} \frac{\partial q^*}{\partial T} (T_{\mathrm{air}} - T_g)], \quad (5)$$

where $q^*(T)$ follows the Clausius–Clapeyron relationship. With fixed RH, near the standard pressure and temperature (i.e., 1013.25 hPa and 273 K), the water vapor in the atmosphere will increase 20% for every 3-K temperature increase (Hartmann 1994). However, the temperature difference between T_{air} and T_g is always small. From observations (Peixoto and Oort 1992), the difference is less than 1 K in most parts of the ocean over the year except in the western boundary of the Pacific and Atlantic Oceans. In our model, the air–sea temperature difference is much smaller than 1 K (results not shown here). Thus, the contribution of the second term to the latent heat flux is much smaller than the first term in Eq. (5). The latitudinal distribution of the latent heat flux mainly depends on the contribution from the undersaturation of the surface air and is primarily determined by the surface temperature distribution.

4. The role of the boundary layer processes

The spinup runs have shown that the eddy mixing of the surface air temperature can greatly influence the equilibrium state surface temperature by modifying the surface sensible heat flux. As shown in Z09, boundary layer processes strongly affect the lower atmosphere eddy activity. Meanwhile, boundary layer processes, especially the surface heat fluxes, also strongly contribute to the surface temperature variation. How do the boundary layer processes influence the equilibration of the coupled system? What is the mechanism through which different boundary layer processes prevent the PV homogenization in the coupled system? We discuss these questions in this section by carrying out sensitivity studies to the strength of surface sensible and latent heat flux (''tcd'' runs), boundary layer thermal diffusion (''snu'' runs), and surface friction (''fcd'' runs). The parameters used in these runs are listed in Table 1. Because the meridional gradient of the temperature is the key factor that determines the eddy equilibration, the horizontal averaged surface temperature is kept fixed[1] in the sensitivity runs in order to explore a wider range of the boundary layer parameters. Thus, in the plots of surface temperature and surface energy flux in this section, the horizontal average of each field is subtracted. For the experiments on surface

[1] Experiments including the variation of the horizontal averaged surface temperature were also carried out. The horizontal averaged surface temperature shows strong variation only in the sensitivity runs to c_{dt}. In those runs, a weak enough c_{dt} results in strong surface warming, in which the surface latent heat flux becomes much more sensitive to the temperature variation. In that situation, moist physics in the atmosphere should play a more important role, which is out of the scope of this study.

TABLE 1. Values of the boundary layer coefficients used in the SD, tcd, snu, fcd, and fcd_{ge} runs, and the statistics of the equilibrium state surface temperature gradient and eddy heat fluxes averaged over the boundary layer at the center of the channel in these runs. The blank means that the value of the coefficient is the same as in the SD run.

Run	c_{dt} (m s^{-1})	μ_s (m^2 s^{-1})	c_{df} (m s^{-1})	With ageostrophic winds	dT_g/dy [K (1000 km)$^{-1}$]	$[v^*T^*]_{bl}$ (K m s^{-1})	$[\omega^*T^*]_{bl}$ (K Pa s^{-1})
SD	0.03	5	0.03	Yes	−13.5	17.8	−0.20
tcd runs							
tcd0	0.00				−23.4	14.3	−0.15
tcd1	0.01				−20.5	24.7	−0.31
tcd6	0.06				−9.1	7.3	−0.11
snu runs							
snu0		0			−15.5	15.7	−0.13
snu2		2			−13.7	17.1	−0.19
snu10		10			−13.5	17.9	−0.21
fcd runs							
fcd6			0.06		−14.6	15.6	−0.22
fcd12			0.12		−14.9	15.5	−0.25
fcd_{ge} runs							
SD_{ge}				No	−13.4	11.6	−0.16
$fcd1_{ge}$			0.01	No	−11.6	14.6	−0.11
$fcd6_{ge}$			0.06	No	−18.3	8.7	−0.17

friction, an additional group of simulations is carried out to compare with the uncoupled run results in Z09, in which only the frictional forcing by geostrophic winds is considered ("fcd_{ge}" runs). Here we did not run the sensitivity test for the boundary layer vertical momentum diffusion. As indicated in Z09, the equilibrium state in the atmospheric model varies only slightly with the momentum diffusion and is not a process that directly influences the surface heat budget. Thus, it is not expected to be an important process that influences the coupled system. In all of these experiments, we take the calibrated state surface temperature distribution and the corresponding RCE state as the initial state, still with small-amplitude perturbations in zonal wavenumbers 1–10 added at the initial moment. We run the experiments for 3000 days with the statistics taken over the last 1000 days.

The latitudinal distributions of the equilibrium state surface temperature in the four groups of experiments are plotted in Fig. 3. The equilibrium state eddy heat fluxes averaged over the boundary layer are also listed in Table 1. From Fig. 3, we find that the surface temperature gradient is most sensitive to the surface heat flux, with stronger c_{dt} resulting in a weaker surface temperature gradient, which is consistent with the fact that surface latent and sensible heat fluxes are the most important components to balance the solar radiation. When the surface heat fluxes are turned off (i.e., when $c_{dt} = 0$ m s^{-1}), the temperature contrast across the channel reaches as large as 64 K in the equilibrium state. Boundary layer thermal diffusion, which is not a direct term in the surface energy budget, only affects the surface temperature slightly. Thus, in the coupled runs the atmospheric flow varied in the same trend with μ_s as in the uncoupled runs in Z09 (as indicated in Table 1). Surface friction, though not a direct component in the surface energy balance, shows an obvious influence on the surface temperature distribution, with weaker surface friction resulting in weaker surface temperature gradient in the equilibrium state. The net effect of including the surface friction by ageostrophic winds is similar to reducing the surface drag coefficient, which also reduces the sensitivity of the surface temperature on the surface friction. In this section, we will investigate the detailed mechanisms through which surface heat flux and friction influence the equilibration of the coupled system as well as the PV homogenization.

a. Surface sensible and latent heat exchange

The surface heat drag coefficient is a parameter that represents both surface sensible and latent heat flux strength in the coupled model. As shown in the previous section, these are important components in the surface energy budget. They act on the surface air on a very fast time scale (Stull 1988) and strongly influence the boundary layer eddy activity. Their meridional distribution also has different dependence on the lower-level eddy activity and the surface temperature. To better illustrate the mechanism through which surface heat fluxes affect the equilibration, in addition to the equilibrium states in each tcd run, the transient response of the coupled system to the variation of the surface heat flux is also investigated. In appendix C, another group of sensitivity studies varying the value of B_o is also carried out to understand the relative role of surface sensible and latent heat fluxes.

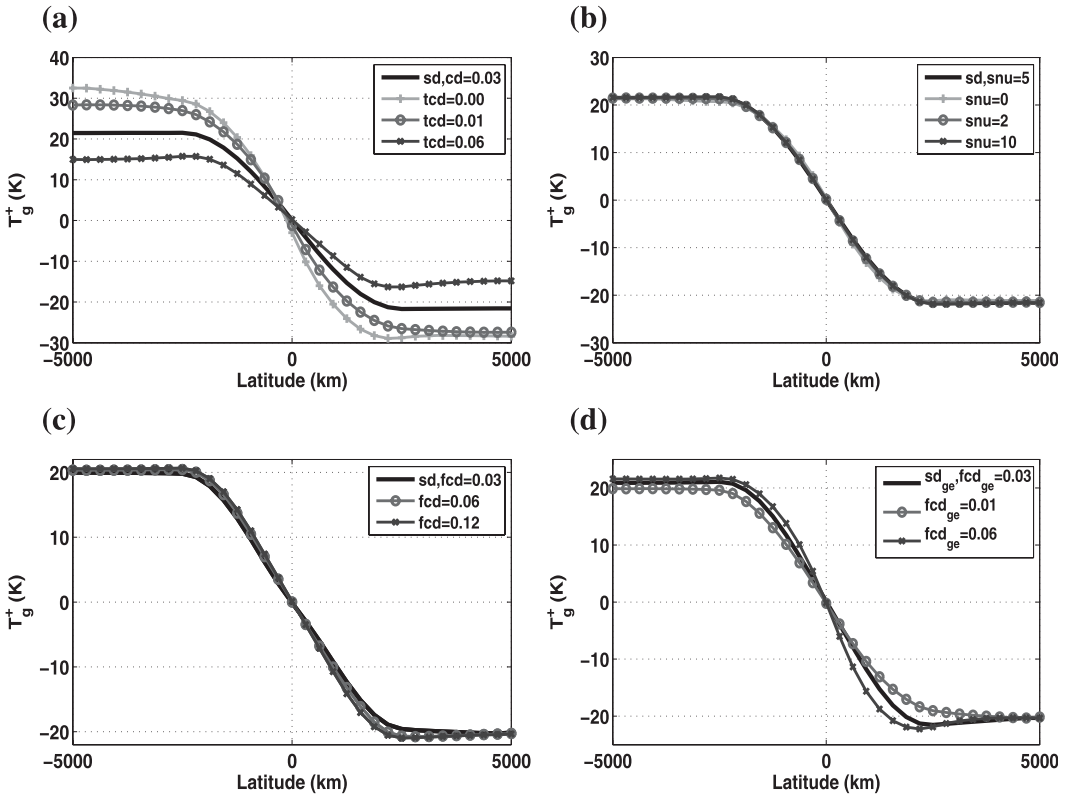

FIG. 3. Latitudinal distribution of the equilibrium state surface temperature anomalies (deviation from the horizontal mean) for the (a) tcd, (b) snu, (c) fcd, and (d) fcd_{ge} runs.

1) EQUILIBRIUM RUNS

The equilibrated state surface energy balance and their variation compared with the SD run are displayed in Fig. 4. Although the meridional surface temperature distribution varies smoothly with c_{dt} as shown in Fig. 3a, two regimes can be observed from Fig. 4 for the surface energy balance. One regime is for nonzero c_{dt}, in which, similar to the SD run in Fig. 2d, the meridional difference of solar radiation over the channel is primarily balanced by the latent heat flux and Q flux, with sensible heat flux and longwave radiation playing secondary roles. The other regime involves turning off latent and sensible heat fluxes, as shown in Fig. 4a, so that longwave radiation plays a more important role. When $c_{dt} = 0$ m s^{-1}, with the enhanced surface temperature gradient, the surface emits more longwave radiation into the atmosphere at lower latitudes, which acts as a negative feedback to balance the exerted differential heating by the solar radiation.

Except for the simulation turning off the surface heat flux, when we increase the surface heat exchange coefficients, the variations of the sensible and latent heat fluxes are in different directions. As shown in Fig. 4c, increasing c_{dt} results in stronger latitudinal variation of latent heat flux; however, it also results in weaker sensible heat flux. The latent heat flux, as discussed in section 3, is mainly determined by the drag coefficient and the surface temperature distribution. Although the drag coefficient is doubled, the equilibrium state temperature gradient is reduced to almost two-thirds of the SD run. Because of this negative feedback, the latitudinal variation of the latent heat flux in the new equilibrium state only increases around 20%. The sensible heat flux, however, equilibrates with a weaker meridional variation under stronger c_{dt} because of the reduced eddy heat flux. This indicates that atmospheric eddy activity is the dominant factor that determines the surface sensible heat flux distribution, whose effect overcomes the direct influence of c_{dt}.

In the atmosphere, the RCE state temperature gradient distribution at the center of the channel, as displayed in Fig. 5a, follows the surface temperature distribution. Stronger surface heat exchange results in a weaker RCE state temperature gradient. The equilibrium state surface air temperature gradient, similar to the uncoupled atmospheric run, is closer to the RCE state as well as the underlying surface temperature gradient under stronger surface heat exchange. However, more complicated than

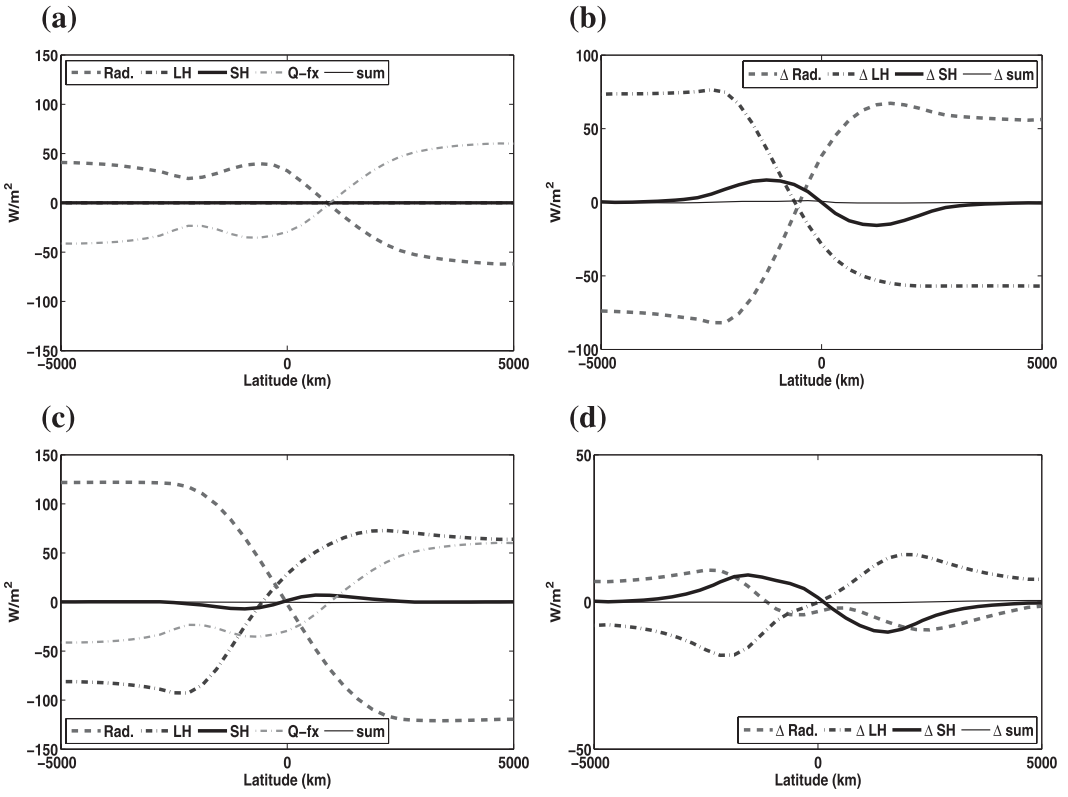

FIG. 4. (a),(c) Latitudinal distribution of the equilibrium state radiative flux, latent heat flux, sensible heat flux, and Q-flux anomalies (deviation from the horizontal mean) in the underlying surface energy budget for the $c_{dt} = 0.00$ and 0.06 m s^{-1} runs, respectively, and (b),(d) the difference of these fluxes anomalies compared with the $c_{dt} = 0.03$ m s^{-1} (SD) run.

the uncoupled atmosphere runs, the variation of c_{dt} in the coupled model, in addition to affecting the atmospheric eddy activity and the mean flow, also influences the RCE state temperature distribution as well as the subsequent radiative–convective heating exerted on the atmospheric flow. The net result of these effects, as shown in Fig. 5a, is that at most levels of the troposphere, the influence of the radiative–convective heating is dominant. Under stronger differential heating, the atmosphere equilibrates at a state with a stronger temperature gradient, and the eddy heat flux also gets stronger as shown in Table 1. One exception is the run where the surface heat flux is turned off, in which, without the surface thermal damping, the temperature gradient near the surface is greatly reduced by the mixing of baroclinic eddies. In the upper troposphere, however, strong temperature gradient is maintained by the strong diabatic forcing. The eddy heat flux shows moderate intensity compared with the runs when c_{dt} is nonzero.

The equilibrium state stratification, as in Eq. (A2), is determined by the eddy vertical heat flux, boundary layer thermal forcing, and radiative–convective heating. Since the RCE state lapse rate is the same in these runs, the first two components are the dominant factors that determine the equilibrium state stratification. Although the vertical eddy heat flux as shown in Table 1 varies nonmonotonically, the flow in Fig. 5b is more stably stratified under weaker c_{dt}.

Although the atmospheric flow equilibrates with a stronger temperature gradient as c_{dt} decreases, the equilibrium state PV gradient, as shown in Figs. 5c and 5d, displays a tendency similar to the uncoupled runs in Z09. In the free troposphere, as shown in Fig. 5c, the PV gradient around 600–850 hPa is still homogenized most when turning off the surface thermal damping. The tendency of the PV gradient to the varying c_{dt} is more obvious in the boundary layer, where the PV gradient is more efficiently mixed for weaker c_{dt} as shown in Fig. 5d.

In our sensitivity study, we include an extreme case in which the surface heat exchange is turned off. In its equilibrium state, the forcing by differential shortwave radiation is primarily balanced by the longwave radiation. The underlying surface stays in a radiative equilibrium-like state. However, with no sensible and latent heat fluxes going into the atmosphere, it would not be a good assumption to have a lapse rate including the convection and moisture effects in the RCE state. Even though

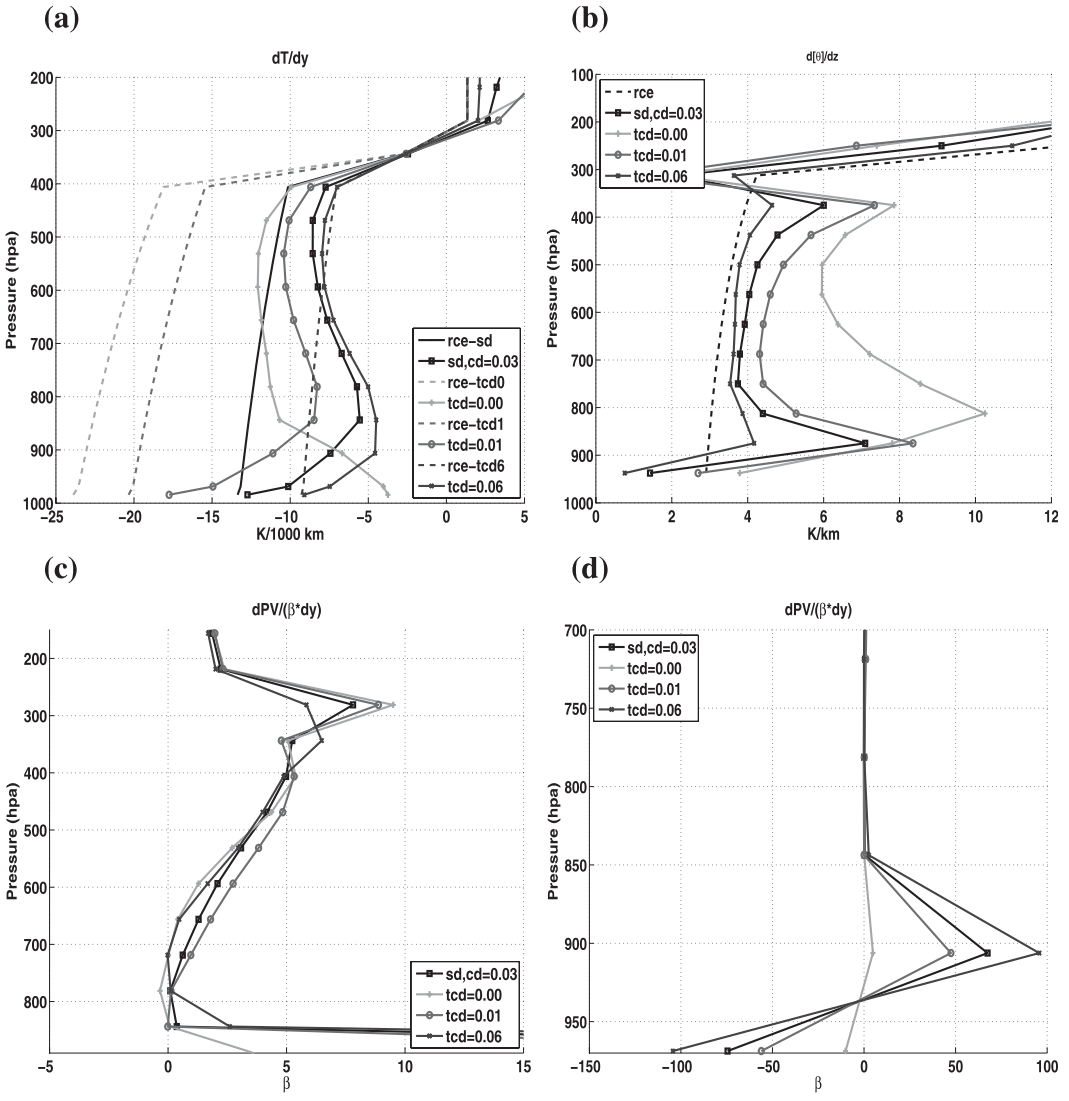

FIG. 5. Vertical distribution of (a) the zonal mean temperature gradient at the center of the channel, (b) stratification, and (c),(d) zonal mean PV gradient, respectively, at the center of the channel in the free troposphere and in the boundary layer in the $c_{dt} = 0$, 0.01, and 0.06 m s^{-1} runs and the SD runs.

losing some physical meaning, this run is still helpful in understanding the role of the surface sensible and latent heat fluxes in the coupled system.

2) TRANSIENT RESPONSE TO SURFACE SENSIBLE AND LATENT HEAT EXCHANGE

To better understand the response of the coupled system to the variation in the surface heat exchange, a transient response run is also carried out. Here we start from the equilibrium state of the SD run and suddenly increase c_{dt} from 0.03 (SD) to 0.06 m s^{-1} at the initial moment. The transient response of the surface energy fluxes and the surface temperature are plotted in Fig. 6. The time evolution of the poleward eddy heat flux and the meridional temperature gradient in the boundary layer are also plotted in Fig. 7.

The immediate response to the sudden increase in c_{dt}, as shown in Figs. 6a and 6b, is an increase in the surface sensible and latent heat fluxes. Compared with the SD run distribution in Fig. 2d, their meridional variations are doubled with c_{dt} at the initial moment. However, with the strong surface heat drag coefficient, the enhanced sensible heat flux quickly disappears. After day 1, it even becomes smaller than in the SD run. From Eq. (A4), this must be due to the greatly reduced air–sea temperature difference under the stronger surface flux. This quick adjustment time scale of the sensible heat flux is also consistent with the scale analysis in Z09 that the

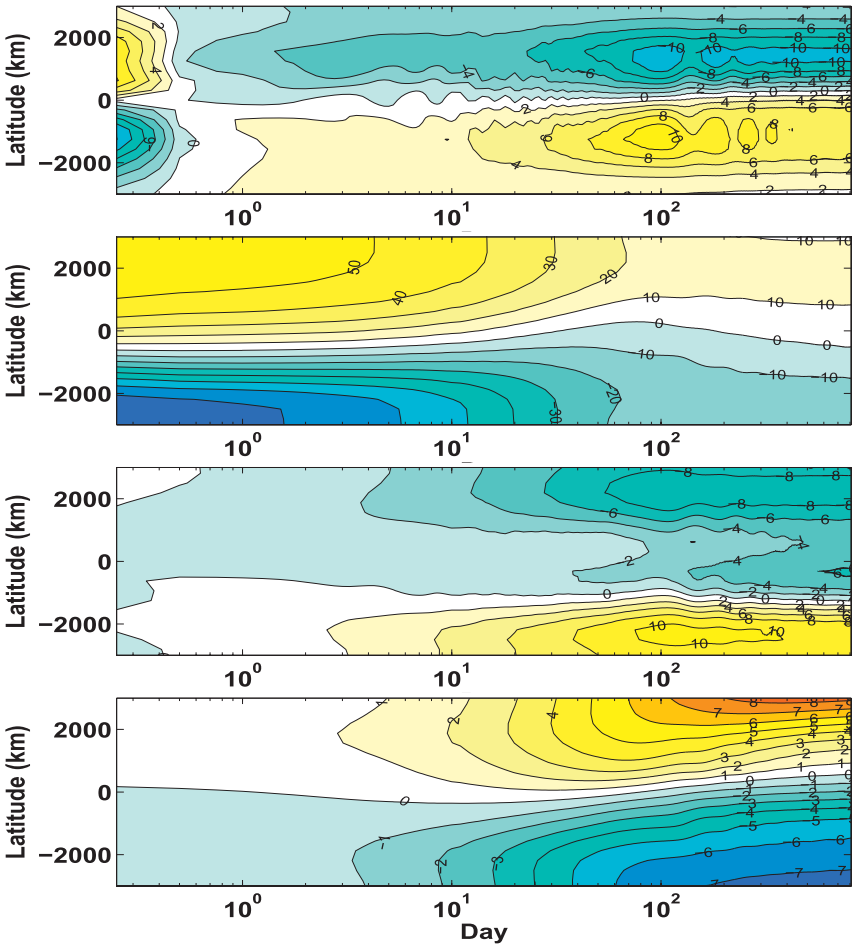

FIG. 6. Time evolution of the (a) sensible heat flux variation $F_{sh} - \overline{F_{sh}}^{sd}$, (b) latent heat flux variation $F_{lh} - \overline{F_{lh}}^{sd}$, (c) radiative flux variation $F_{rad} - \overline{F_{rad}}^{sd}$, and (d) surface temperature variation $T_g - \overline{T_g}^{sd}$ when suddenly increasing c_{dt} from 0.03 (SD) to 0.06 m s^{-1}, where $\overline{\cdots}^{sd}$ means the equilibrium state values in the SD run. Contour intervals are 2, 10, and 2 W m^{-2} in (a)–(c), respectively, and 1 K in (d). Note that the x coordinate is plotted on a logarithmic scale.

response time scale of the surface air to the surface heat flux forcing is around 1 day.

The later response of the latent heat flux is associated with the surface temperature variation. As shown in Fig. 6d, under the stronger surface latent heat flux, the surface temperature begins to change after around 10 days. With the reduced surface temperature gradient, the enhanced latent heat flux starts decreasing. The longwave radiation, as the surface temperature changes, also changes to offset the anomalous latent heat flux. After hundreds of days, the surface energy budget reaches another equilibrium with reduced meridional gradients of the surface temperature, sensible heat flux, and radiative flux but enlarged latent heat flux meridional gradient, which is consistent with Fig. 4d.

The transient response of the atmospheric flow is also shown in Fig. 7. As in the uncoupled run in Z09, the immediate response of the baroclinic eddy to the increase in c_{dt} is a decrease in its magnitude, then the eddy heat flux begins to increase back in the next few days. Around day 7, it even gets slightly stronger compared with the SD run. Similar to the uncoupled run, this is primarily because as the surface air is dragged closer to the surface temperature, the boundary layer temperature gradient becomes stronger as well. However, as the surface temperature gradient begins to decrease in response to the doubled latent heat flux, the lower-level temperature gradient is also reduced. With a few days lag, the eddy heat flux also begins to decrease. After around a hundred days, the eddy heat flux is reduced to less than one-fourth of its original value and stops decreasing. The eddies and the zonal flow experience negatively correlated oscillations. After hundreds of days, the atmospheric flow and the surface reach a quasi-equilibrium state with

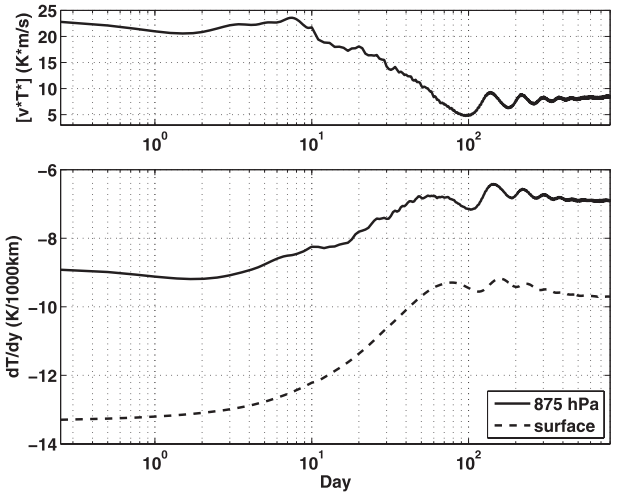

FIG. 7. (top) Time evolution of the boundary layer averaged poleward eddy heat flux and (bottom) the surface and 875-hPa temperature gradients at the center of the channel when suddenly increasing c_{dt} from 0.03 (SD) to 0.06 m s^{-1}. Note that the x coordinate is plotted on a logarithmic scale.

a weaker zonal flow baroclinicity and much weaker eddy activity.

As mentioned in section 2, to save computation time, a 5-m surface layer depth is used in the transient response experiment. This is a much shallower surface layer compared with the depth of the ocean mixed layer in midlatitudes. Nevertheless, the transient response of the coupled model still clearly displays the different response time scales on which different processes affect the equilibration of the coupled system. The boundary layer process works on the lower atmosphere on a very quick time scale (~1 day). Baroclinic eddies respond to the variation in the mean flow on a time scale of a few days. The underlying surface's response time scale to the variation of the surface heat flux is dependent on the surface layer depth. In this experiment, its response time scale is hundreds of days. These processes work together to maintain the equilibrium of the coupled system.

b. Surface friction

In a thermally coupled model, surface friction does not affect the surface energy balance directly but exerts the influence by modifying the atmospheric eddy activity. In addition, as shown in Fig. 3d, the nonmonotonic response of the equilibrium state to the varying c_{df} in Z09 does not occur in the coupled system. To understand these responses, the details of fcd_{ge} runs are investigated.

1) EQUILIBRIUM STATE

The equilibrium state atmospheric temperature gradient, heat fluxes, and PV gradient distributions are displayed in Fig. 8. The latitudinal distribution of each surface energy flux in the equilibrium state and their variation compared with the SD run when under weaker (c_{df} = 0.01 m s^{-1}) surface friction are also plotted in Fig. 9. As shown in Figs. 8 and 9, compared to Z09, surface friction affects the eddy and the mean flow of the coupled system in more complex ways.

1) The RCE state temperature gradient in the atmosphere, as a consequence of the reduced underlying surface temperature, gets weaker as the surface friction is reduced. Different from Z09, the equilibrium state atmospheric temperature exhibits a monotonic variation with c_{df}; that is, as shown in Fig. 8a, a weaker meridional temperature gradient is obtained under a weaker surface friction.
2) The response of the meridional eddy heat flux in Fig. 8b, however, may differ from one's expectation. When c_{df} = 0.01 m s^{-1}, in spite of the weaker baroclinicity of the mean flow, the eddy heat flux gets stronger compared with the SD run. This indicates that under the competing effects of the weaker mean available potential energy and the weaker frictional damping on the eddy energies, the later effect dominates. The vertical eddy heat flux as shown in Table 1, however, varies weakly and in an opposite direction to the meridional eddy heat flux, which indicates that surface friction also strongly influences the eddy mixing slope in the equilibrium state.
3) The variation of the equilibrium state PV gradient, as shown in Figs. 8c and 8d, along with the temperature gradient, is also monotonic with c_{df}. In both the boundary layer and the free troposphere, PV equilibrates with a smaller meridional gradient as the surface friction becomes weaker.
4) Similar to the tcd runs, the variation of the latent heat flux is balanced by the sensible heat flux and radiative flux. The sensible heat flux gets stronger with weaker c_{df}. However, the variation of each energy flux is confined in the central half of the channel, where the eddy heat flux is most active, indicating that the variation of the surface energy fluxes is eddy induced.

It is worthwhile to point out that above variation trends with changes in surface friction still hold in the fcd runs as shown in Table 1, only with the magnitude of variation becoming weaker, which shows the robustness of the results we obtained.

2) TRANSIENT RESPONSE

A transient response experiment is also carried out to further investigate the mechanism through which surface

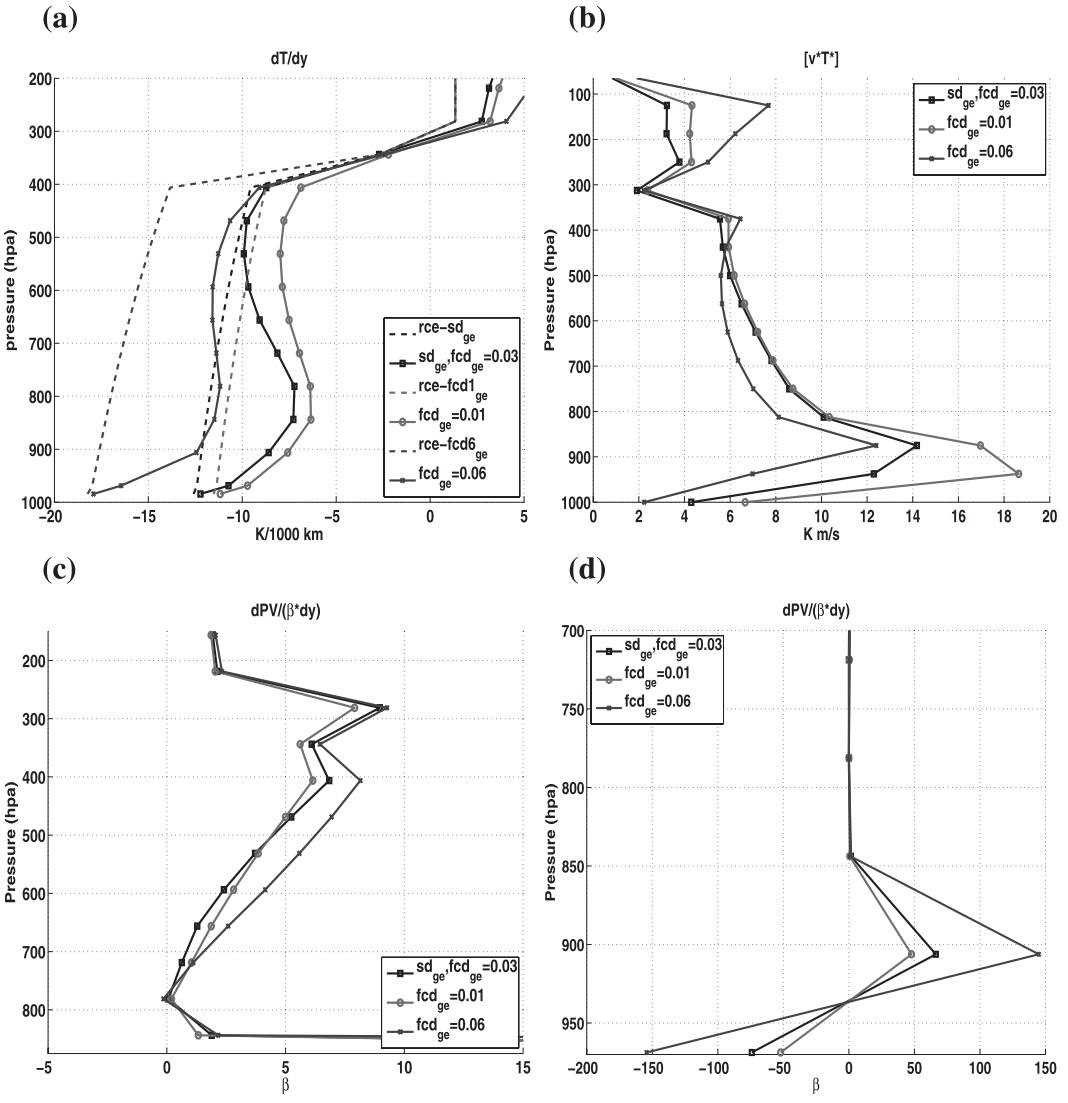

FIG. 8. Vertical distribution of the equilibrium state (a) meridional temperature gradient (solid curves) and the corresponding RCE state temperature gradient (dashed curves), (b) eddy poleward heat flux, and (c),(d) meridional PV gradient, respectively, in the free troposphere and in the boundary layer at the center of the channel for the c_{df} = 0.03 (SD run), 0.01, and 0.06 m s^{-1} runs.

friction influences the coupled system. In the experiment, we also start from the equilibrium state of the SD run and suddenly reduce c_{df} from 0.03 to 0.01 m s^{-1}. The time evolution of each surface energy flux and the surface temperature variation are plotted in Fig. 10. The transient response of the poleward eddy heat flux in the boundary layer and the temperature gradient at surface as well as 875 hPa at the center of the channel are also displayed in Fig. 11. In these plots, we can clearly see three response time scales of the coupled system to the reduced surface friction: a synoptic adjustment time scale (first a few days), a nonlinear adjustment time scale of the atmospheric flow (tens of days), and an underlying surface response time scale, which depends on the surface heat content (hundreds of days in our model).

The immediate response to the reduced surface friction lies in the poleward eddy heat flux and the temperature gradient in the atmospheric boundary layer. The eddy heat flux increases to twice its original value in the first few days. The lower-level temperature gradient, following the variation of the eddy heat flux, is also strongly reduced, along with which the surface sensible heat flux is greatly enhanced in the first few days, with a peak at day 7 as shown in Fig. 10. Then, as shown in Fig. 11, the boundary layer temperature gradient stops decreasing and begins to increase quickly, which, as in Z09,

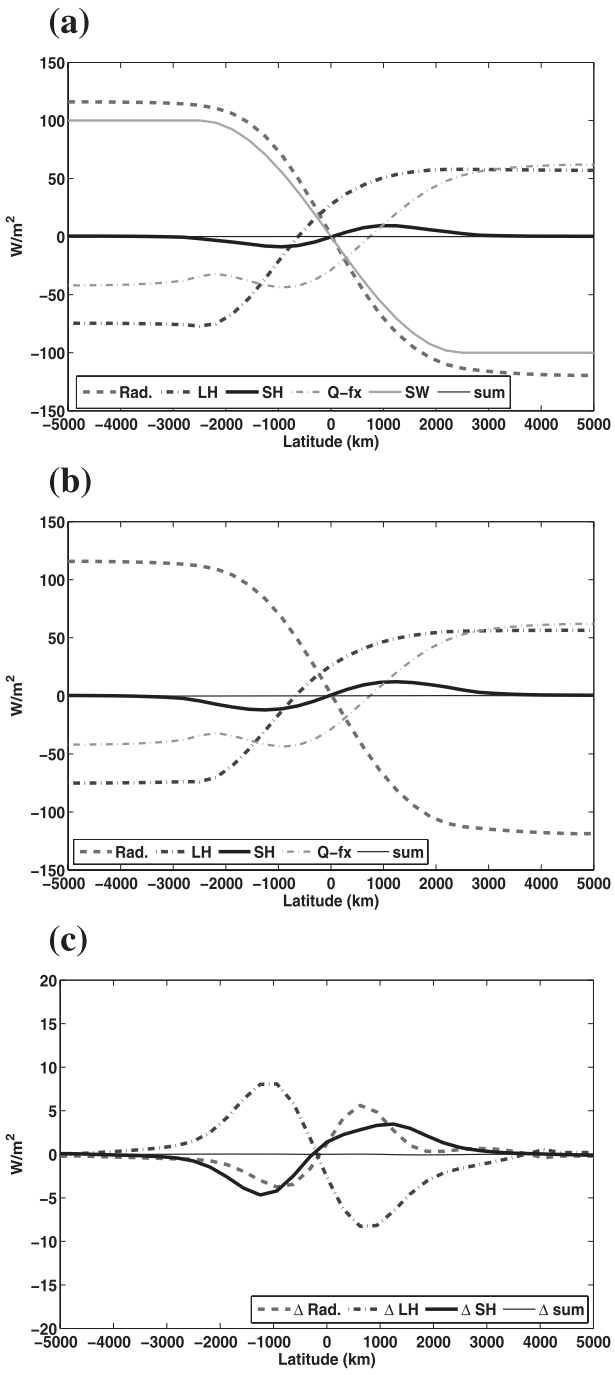

FIG. 9. Latitudinal distribution of the equilibrium state radiative flux, latent heat flux, sensible heat flux, and Q-flux anomalies in the underlying surface energy budget for the (a) SD_{ge} and (b) $fcd1_{ge}$ runs, and (c) the difference of the flux anomalies in the $fcd1_{ge}$ run compared with the SD_{ge} run.

is mainly because the latitudes where the temperature is most modified by the baroclinic eddies move away from the center of the channel, with the temperature gradient at the center not being efficiently reduced but more modified at the flanks of the jet. This is also clearly seen in Fig. 10a, in which the latitudes where the surface sensible heat flux is most modified also move away from the center of the channel. This is consistent with the nonmonotonic response to the surface friction in the uncoupled run in Z09. Such a nonlinear adjustment time period of the atmospheric eddy–mean flow system lasts to day 30.

With the enhanced sensible heat flux, the surface temperature gradient at the center of the channel also begins to decrease. The meridional variation of latent heat flux is reduced with the surface temperature gradient, which acts to offset the increase in sensible heat flux. The longwave radiation anomaly also appears to reduce the surface temperature gradient. In this period, surface temperature, atmospheric temperature, and the eddy heat flux show different correlations from the synoptic adjustment period. As the surface temperature gradient is further reduced, the boundary layer temperature gradient and the eddy heat flux also become weaker. After hundreds of days, the coupled system reaches an equilibrium state with a strongly reduced surface and atmospheric temperature gradient. The eddy heat flux, despite becoming weaker in the last few hundreds of days with the weaker mean flow temperature gradient, still equilibrates at a stronger state than the SD run.

5. Summary and discussion

In this study, baroclinic eddy equilibration and the roles of different boundary layer processes in limiting the PV homogenization are investigated using an atmosphere–ocean thermally coupled model to extend our understanding of the baroclinic adjustment to the air–sea coupled system. In the coupled system, the existence of baroclinic eddies enhances the surface sensible heat flux and acts to reduce the surface baroclinicity. The schema for this mechanism is illustrated in Fig. 12. As shown in the spinup runs, without baroclinic eddies, surface thermal damping, which can quickly eliminate the difference between the surface and surface air temperature, is the dominant process that determines the surface air temperature distribution, resulting in weak surface sensible heat flux. By mixing the surface air temperature, baroclinic eddies, as shown in Fig. 12, act to compete the surface thermal damping and increase the difference between θ_{air} and θ_g. Thus, stronger surface sensible heat flux is obtained when baroclinic eddies are present.

Furthermore, our sensitivity studies show that the distribution of the surface sensible heat flux is in fact most dependent on the eddy activity of the surface air, with stronger meridional variation of the surface sensible heat flux accompanied with stronger atmospheric eddy activity. Even in the sensitivity runs to the surface

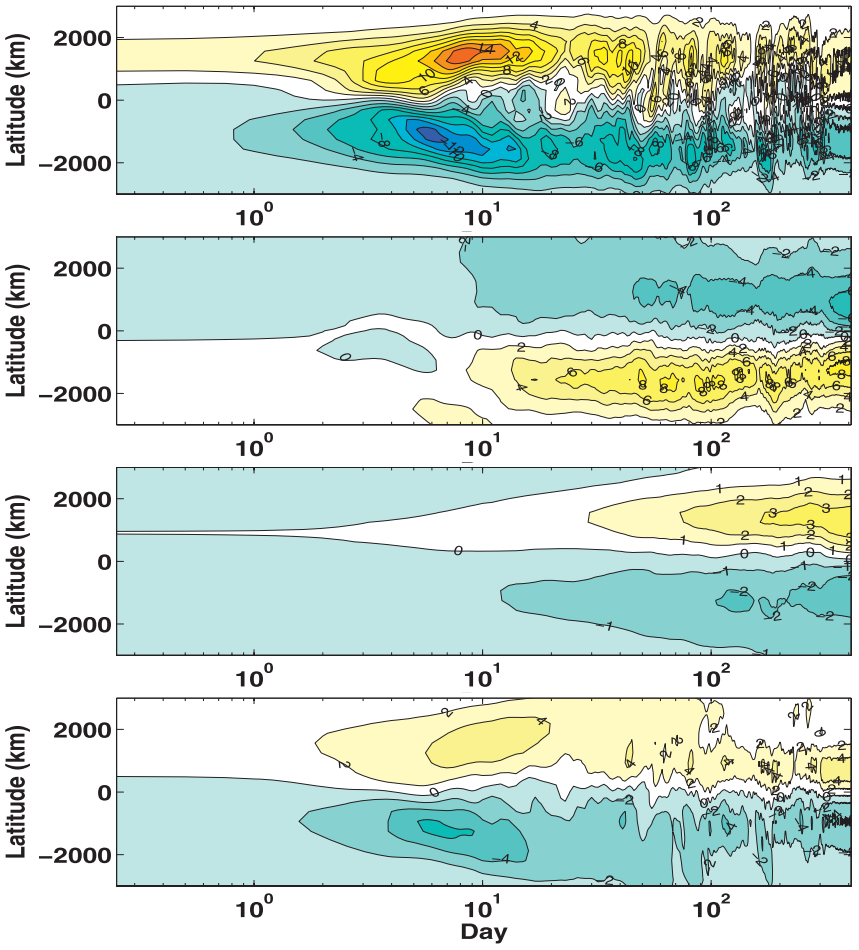

FIG. 10. As in Fig. 6, but for c_{df} reduced from 0.03 (SD) to 0.01 m s^{-1}. Contour intervals are 2, 2, and 1 W m^{-2} in (a)–(c), respectively, and 2 K in (d).

heat flux, a stronger sensible heat drag coefficient, however, results in weaker surface sensible heat flux because of the weaker eddy activity in the atmosphere. This helps explain that the observed surface sensible heat flux and the surface heat flux feedback is always strongest in the storm track region in cool seasons (Cayan 1992; Frankignoul and Kestenare 2002; Yu et al. 2009). This dependence also indicates that, different from the latent heat flux, the sensible heat flux is determined nonlocally. The distribution of the surface latent heat flux, however, as discussed in section 3, is primarily a function of local SST; thus, its variation is always in phase with the SST anomaly in the simulations, which also occurs in the GCM runs (Kushnir and Held 1996). Their different dependence explains why in the spinup runs and sensitivity runs, surface sensible and latent heat fluxes can vary in different directions. The different dependence of the sensible and latent heat fluxes may also bring insight into the disparity of the GCMs results on the surface heat flux feedback (Peng et al. 1995; Frankignoul et al. 2004).

Although baroclinic eddies can act to reduce the surface baroclinicity, the requirement of the surface energy balance indicates that strong surface temperature gradient is always maintained in response to the strong meridional variation of the solar radiation. Our sensitivity study investigates different cases of surface energy balance. Over the ocean surface, the balance between the meridional variation of latent heat flux and solar radiation indicates that strong surface baroclinicity is always required. As a rough estimation, the difference of the energy fluxes over the central half of the channel: $\delta(\mathrm{SW} - Q_{\mathrm{fx}}) \sim \delta F_{\mathrm{lh}} \sim c_{dl} L \rho_s (1 - \mathrm{RH}) \delta q^*(T_g)$. The baroclinicity of the underlying surface δT_g strongly depends on the drag coefficient c_{dl} and $\partial q^*/\partial T$. For the dry limit in which the sensible heat flux plays the dominant role and for the case where the energy balance is between the solar and longwave radiation, strong surface

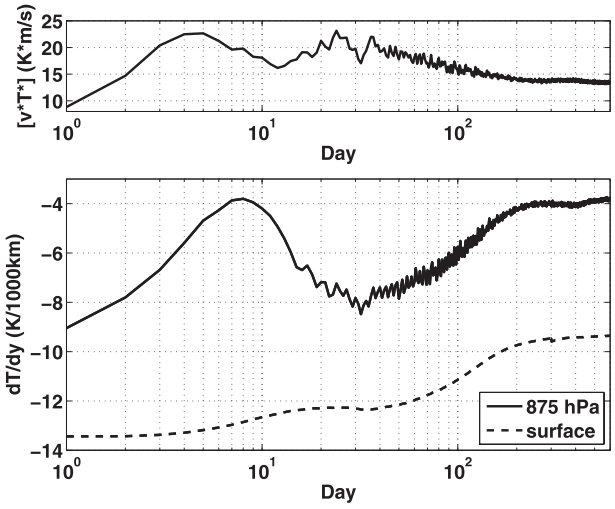

FIG. 11. As in Fig. 7, but reducing c_{df} from 0.03 (SD) to 0.01 m s^{-1}.

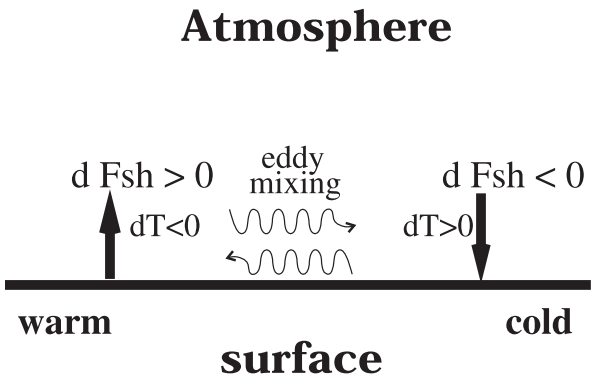

FIG. 12. A schematic map showing how eddy mixing influences the surface sensible heat flux.

baroclinicity are all demanded. With the strong surface meridional temperature gradient and the boundary layer processes, the PV homogenization in the boundary layer is always suppressed. The homogenized PV gradient as suggested by the baroclinic adjustment (Stone 1978; Gutowski 1985; Lindzen 1993) will never be observed near surface or in the boundary layer (Stone and Nemet 1996; Kirk-Davidoff and Lindzen 2000).

As shown in the study, the equilibration of the coupled system involves more dynamical feedbacks and time scales, and different boundary layer processes influence the equilibrated states differently. However, the response of the PV gradient to changes in the boundary layer processes is very robust. In the boundary layer, the PV structure responds to different boundary layer processes in a more uniform way compared with the uncoupled runs in Z09; that is, the PV homogenization is more efficiently limited under the stronger boundary layer forcing. This tendency even holds in the sensitivity runs to surface heat flux. In the coupled run, reducing the surface heat drag coefficient results in much stronger surface and atmospheric temperature gradients. However, a weaker PV gradient is obtained in the boundary layer under the weaker surface thermal damping. This shows that the strength of the boundary layer damping is the most dominant factor that determines the PV distribution there. In the free troposphere, the PV distribution is relatively robust with homogenized PV around 600–800 hPa in all the simulations, which indicates the effect of baroclinic adjustment (Zurita and Lindzen 2001; Zurita-Gotor and Lindzen 2004a).

In the atmosphere–ocean thermally coupled model used in this study, heat transport by oceanic dynamics is represented with a precalculated Q flux. The variation of the oceanic heat transport caused by the boundary layer processes is neglected. Although, as reviewed by Frankignoul (1985), surface heat fluxes are the dominant heating for the SST variation especially in fall and winter, the slab ocean model is a good assumption only as long as the variation time scale of the oceanic heat transport is much longer than the other surface energy fluxes. For decadal–interdecadal climate variability of the midlatitude coupled system, horizontal heat transport by upper-ocean currents plays an important role in the SST variation, in which the change in surface wind stress can excite the oceanic Rossby waves (Jin 1997; Neelin and Weng 1999; Schneider et al. 2002) and result in the slow adjustment of the oceanic gyre circulation (Jin 1997; Seager et al. 2001; Lee et al. 2008). The meridional overturning circulation in the ocean, which also contributes to the decadal–interdecadal climate variability, especially in the North Atlantic, is associated with the surface heat and momentum fluxes as well (Delworth and Greatbatch 2000; Dong and Sutton 2005). When taking into account these oceanic dynamics, how the boundary layer processes influence the decadal–interdecadal variability of the coupled system could be another interesting topic. In addition, the atmospheric model used in this study is a dry process model. The effect of condensational heating, combined with the radiative forcing, is simply considered by a Newtonian cooling, in which the moist physics are not included. Given that condensational heating is an important component in the midlatitude circulation (Trenberth and Stepaniak 2003), the influence of the moist dynamics on the baroclinic adjustment needs further studies. The role of the boundary layer processes, especially the surface evaporating cooling, in the baroclinic eddy equilibration needs further investigated in a moist model.

Acknowledgments. Most of the work in this study was carried out during the first author's Ph.D. study at MIT,

where both authors were supported by the Office of Science (BER), U.S. Dept. of Energy, Grant DE-FG02-93ER61677, and by the Goddard Institute for Space Studies, under NASA Cooperative Agreement NNG04GF12A. The first author was also supported by the National Nature Science Foundation of China (NSFC) under Grant 41005028.

APPENDIX A

Atmospheric Model Description

In our β-plane multilevel quasigeostrophic model, the variables are defined in gridpoint space. The horizontal resolution of the model is 330 km in both zonal and meridional directions. The model has 17 equally spaced levels. As shown by Solomon and Stone (2001a), this resolution is good enough to simulate the eddy dynamics. In addition, an FFT filter is used on the streamfunction to remove the smallest-scale eddies.

a. Governing equations

In this model, the potential vorticity equation, including diabatic heating and boundary layer dissipation, is integrated:

$$\frac{\partial q}{\partial t} = -J(\psi, q) - f_o \frac{\partial}{\partial p}\frac{QR}{spc_p} + \mathbf{k}\cdot\nabla\times\mathbf{F}, \qquad \text{(A1)}$$

where $R = 287$ J kg^{-1} K^{-1} is the ideal gas constant, $c_p = 1004$ J kg^{-1} K^{-1} is the specific heat of the air, and ψ is the geostrophic streamfunction. The static stability parameter $s = -(1/\varkappa)(\partial\overline{\theta}^{xy}/\partial p)$, where $\overline{\cdots}^{xy}$ means averaged horizontally, $\varkappa = (p/R)(p_o/p)^{R/c_p}$, and p_o is the surface pressure. Also, $\mathbf{F}$ denotes the frictional dissipation and the diabatic heating term Q has two contributors: radiative–convective heating Q_r and the thermal diffusion in the boundary layer Q_d. The potential vorticity is $\mathrm{PV} = \nabla^2\psi + \beta y + (\partial/\partial p)(f_o^2/s)(\partial\psi/\partial p)$, where the Coriolis parameter at the center of the channel is $f_o = 1.03 \times 10^{-4}$ s^{-1}, and the variation of the Coriolis parameter with latitude is $\beta = 1.76 \times 10^{-11}$ m^{-1} s^{-1}. These are the values at latitude 45°N. Under the QG assumption, $\theta^\dagger = -\varkappa f_o(\partial\psi/\partial p)$, where $\theta^\dagger = \theta - \overline{\theta}^{xy}$ indicates the deviation from the horizontal mean. Thus, Eq. (6) only predicts the time evolution of $\theta^\dagger$.

One important difference between this model and traditional QG models is that the horizontally averaged potential temperature and static stability, instead of being specified, are allowed to evolve with time according to the equation

$$\frac{\partial}{\partial t}\overline{\theta}^{xy} = -\frac{\partial}{\partial p}\overline{\omega^*\theta^*}^{xy} + \overline{\frac{Q_r + Q_d}{c_p}}^{xy}\left(\frac{p_o}{p}\right)^{R/c_p}, \qquad \text{(A2)}$$

where the superscript asterisk indicates the eddy component of the variable.

Since the heat exchange between the atmosphere and the surface is considered in the model, a surface air temperature distribution is needed in the surface heat flux estimation. In the atmospheric model, surface air temperature is calculated at the midlevel between the surface and the first model level. The surface air tendency equation, derived from the QG thermodynamic equation, is

$$\frac{\partial T_{\mathrm{air}}}{\partial t} = -J(\psi_{1/2}, T_{\mathrm{air}}) + \frac{Q}{c_p},$$

where $\psi_{1/2} = (\psi_o + \psi_1)/2$, and Q is also estimated at the midlevel between the surface and the first model level.

b. Radiative–convective heating

Radiative–convective heating in this model is parameterized by the Newtonian cooling form:

$$Q_r = c_p\frac{T_e - T}{\tau_r}, \qquad \text{(A3)}$$

where T_e is the atmospheric temperature in the radiative–convective equilibrium (RCE) state corresponding to the surface temperature, and $\tau_r = 40$ days is the relaxation time scale. Since the eddy activity in the atmospheric model is mainly determined by the flow baroclinicity, the global averaged surface temperature in our model is set to be 280 K, and the lapse rate $d\overline{T_e}^{xy}/dz$ of the RCE state is chosen to be -7 K km^{-1} in the troposphere and 0 K km^{-1} in the stratosphere. In this study, the meridional distribution of the potential temperature of the RCE state in the troposphere is set to match the surface temperature T_g by assuming that $\theta_e^\dagger(y,p) = T_g^\dagger(y)$. In the stratosphere, the potential temperature gradient of the RCE state is also one-tenth of that in the troposphere and of the opposite sign. In our channel model, to avoid the influence of lateral boundaries, the baroclinic zone is centered over the central half of the channel in the experiments.

c. Thermal diffusion in the boundary layer

The surface heat exchange between atmosphere and ocean is represented by the linearized bulk aerodynamic drag formula:

$$F_{\rm sh} = -c_{dt} c_p \rho_s (\theta_{\rm air} - \theta_g), \tag{A4}$$

where $c_{dt} = c_{\rm surface}|\nu_s|$ is the drag coefficient. In this study, c_{dt} is chosen to be constant, and 0.03 m s^{-1} is taken as its standard value.

Above the surface, the vertical turbulent heat flux in the boundary layer is parameterized in the diffusive form

$$F_{\rm sh} = \nu_S(p) c_p \rho^2 g \frac{\partial \theta}{\partial p}, \tag{A5}$$

where, as in Zhang and Stone (2010), the vertical thermal diffusion is confined in the boundary layer with

$$\nu_S(p) = \mu_s \left(\frac{p - p_{\rm bl}}{p_o - p_{\rm bl}} \right)^3 \ {\rm m}^2 \ {\rm s}^{-1}, \tag{A6}$$

for $p \geq p_{\rm bl}$, and with $\nu_S(p) = 0$ for $p \leq p_{\rm bl}$, where $p_{\rm bl} =$ 850 hPa is the pressure at the top of the boundary layer and 5 m^2 s^{-1} is taken to be the standard value for μ_s. Heating by thermal diffusion is calculated from the heat flux:

$$Q_d = g \left(\frac{p}{p_o} \right)^{R/c_p} \frac{\partial F_{\rm sh}}{\partial p}. \tag{A7}$$

Here we want to point out that because of the vertical turbulent heat transport, the stratification in the boundary layer can be weak. However, this merely means that the vertical temperature advection by the flow is small and the horizontal temperature advection in this case is dominant. Thus, the QG scaling still holds.

d. Frictional dissipation in the boundary layer

The parameterization of friction is analogous to thermal diffusion $\mathbf{F} = g(\partial \tau_m / \partial p)$, where τ_m is the shear stress and is parameterized by a linearized bulk aerodynamic drag at the surface and vertical diffusion in the boundary layer:

$$\tau_m = -c\, df \rho_s \mathbf{v} \ \text{(surface)}, \tag{A8}$$

$$\tau_m = \nu_M(p) \rho^2 g \frac{\partial \mathbf{v}}{\partial p} \ \text{(boundary layer)}, \tag{A9}$$

where in most experiments $\mathbf{v} = \mathbf{v}_g + \mathbf{v}_a$. Also,

$$\nu_M(p) = \mu_m \left(\frac{p - p_{\rm bl}}{p_o - p_{\rm bl}} \right)^3 \ {\rm m}^2 \ {\rm s}^{-1} \tag{A10}$$

for $p \geq p_{\rm bl}$, and $\nu_S(p) = 0$ for $p \leq p_{\rm bl}$, where $\mu_m =$ 5 m^2 s^{-1} and c_{df} is still chosen to be 0.03 m s^{-1}.

e. Ageostrophic wind in the boundary layer

The effect of ageostrophic winds in the boundary layer is included in this study. The ageostrophic wind in the model is estimated from the Ekman momentum approximation by solving the equation

$$f \mathbf{v}_a = \mathbf{F} = g \frac{\partial \tau_m}{\partial p}.$$

The frictional dissipation caused by the ageostrophic winds is now included. By solving the differential equation with the boundary condition that at the first level,

$$\nu_M(p) \rho^2 g \frac{\partial (\mathbf{v}_g + \mathbf{v}_a)}{\partial p} = -c_{df} \rho_s (\mathbf{v}_g + \mathbf{v}_a),$$

the ageostrophic winds in the boundary layer can be evaluated.

APPENDIX B

The Downward Longwave Radiation

The downward longwave radiation into the surface $F_{\rm lw}^{\downarrow}$ is estimated from the simplified radiative transfer equation. In a gray atmosphere, the radiative transfer equation is simplified as

$$\mu \frac{dI(\mu, \tau)}{d\tau} = I(\mu, \tau) - B(\tau), \tag{B1}$$

where $\mu = \cos\Theta$, Θ is the zenith angle, τ is the optical depth, I is the intensity of radiation, and $B(\tau) = \sigma T(\tau)^4/\pi$ is the blackbody function. The optical depth is specified as a function of pressure and in the model only the two most important absorbing gases, water vapor and CO_2, are considered:

$$\tau = \tau_{\rm H_2O} \left(\frac{p}{p_o} \right)^{\alpha} + \tau_{\rm CO_2} \left(\frac{p}{p_o} \right). \tag{B2}$$

The first term approximates the structure of water vapor in the atmosphere, and $\alpha = H_p/H_a \approx 7$ km/2 km = 3.5, where H_a is the scale height of the water vapor and H_p is the scale height of pressure. The term $\tau_{\rm H_2O}$ is specified linearly proportional to the water vapor mixing ratio of

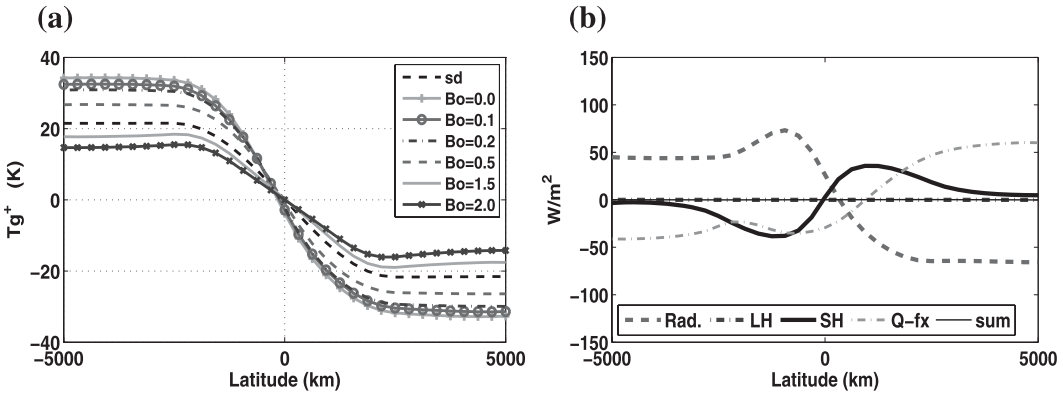

FIG. C1. Latitudinal distribution of the equilibrium state (a) underlying surface temperature when varying the value of B_o and (b) radiative flux, latent heat flux, sensible heat flux, and Q-flux anomalies in the underlying surface energy budget for $B_o = 0$.

the surface air q_{air}. In the standard run, τ_{H_2O} varies from 5.8 at high latitudes to 0.5 at low latitudes. The second term approximates the contribution from CO_2 and we set $\tau_{CO_2} = 1$, a constant in this model. As revealed in Zhang (2009) the influence of CO_2 on the longwave radiation is mainly at high latitudes, which acts to warm the surface temperature there. When $\mu < 0$, $I = I^{\downarrow}$ is the downward radiative intensity. At the top of the atmosphere where $\tau = 0$, $I^{\downarrow} = 0$. Using this boundary condition, we have

$$I^{\downarrow}(\mu, \tau) = -\frac{1}{\mu}\int_0^{\tau} e^{(\tau'-\tau)/\mu} B(\tau')\, d\tau'. \qquad \text{(B3)}$$

Then the downward longwave radiative flux

$$F_{\text{lw}}^{\downarrow}(\tau) = 2\pi\int_{-1}^{0} d\mu \int_0^{\tau} -B(\tau') e^{(\tau'-\tau)/\mu}\, d\tau'. \qquad \text{(B4)}$$

This equation can be simplified mathematically by the two-point Gaussian quadrature, where the optimal abscissas chosen from $-1 \le \mu \le 0$ are $\mu_1 = (\sqrt{1/3} - 1/2)$ and $\mu_2 = (-\sqrt{1/3} - 1/2)$. Thus, at surface, where $\tau = \tau_g = \tau_{H_2O} + \tau_{CO_2}$, the downward longwave radiative flux is simplified as in Eq. (4).

To evaluate Eq. (4), the parameterized downward longwave radiation is compared with a more sophisticated and physical radiation scheme in the column model in Bony and Emanuel (2001), which uses the longwave radiation parameterization of Morcrette (1991). Using the SD state temperature profile, assuming fixed relative humidity, compared with the column model output, Eq. (4) can estimate the downward longwave radiation at the surface of the corresponding latitude reasonably well (Zhang 2009).

APPENDIX C

The Relative Importance of Sensible and Latent Heat Fluxes

In the sensitivity runs in section 4a, the surface energy budget is primarily maintained by the latent heat flux, solar radiation, and the Q flux, which is consistent with the observed ocean surface energy budget. When varying the drag coefficient, the direct effect of the latent heat flux is dominant in determining the surface temperature distribution. However, the sensible heat flux, despite its smaller contribution, is a very active and important component in the storm track region, especially in the Northern Hemisphere. Over land surface, the sensible heat flux has larger magnitude, the contribution of which becomes comparable with the latent heat flux especially in the midlatitudes. In this section, the relative importance of the sensible and latent heat fluxes in determining the surface baroclinicity is studied by varying the B_o coefficient. In the regime of small B_o, surface sensible heat flux plays a more important role, which is similar to the energy balance of land surface.

Surface temperature distributions when varying B_o is displayed in Fig. C1a. In the regime of large B_o, where the latent heat is dominant, the surface temperature is weaker. When B_o is doubled, the surface temperature distribution is similar to the $c_{dt} = 0.06$ run, which is consistent with the weak eddy heat flux and the sensible heat in this case. In the regime of small B_o, a stronger temperature gradient is observed. In this regime, the surface heat budget also shows strong variation.

As shown in Fig. C1b, when the latent heat flux is absent, both the surface sensible heat flux and the longwave radiation become active and act to balance the solar radiation. In this situation, along with the strong

surface baroclinicity and the strong eddy heat flux in the atmosphere (results not shown), the surface sensible heat flux is enhanced. The longwave radiation also behaves as an important component acting to reduce the temperature gradient. Combined with the sensitivity runs in section 4a, strong surface baroclinicity is required in all the situations in response to the meridional variation of the solar radiation.

REFERENCES

Barsugli, J., and D. Battisti, 1998: The basic effects of atmosphere–ocean thermal coupling on midlatitude variability. *J. Atmos. Sci.,* **55,** 477–493.

Bladé, I., 1997: The influence of midlatitude ocean–atmosphere coupling on the low-frequency variability of a GCM. Part I: No tropical SST forcing. *J. Climate,* **10,** 2087–2106.

Bony, S., and K. Emanuel, 2001: A parameterization of the cloudiness associated with cumulus convection; evaluation using TOGA COARE data. *J. Atmos. Sci.,* **58,** 3158–3183.

Branscome, L. E., W. J. Gutowski, and D. Stewart, 1989: Effect of surface fluxes on the nonlinear development of baroclinic waves. *J. Atmos. Sci.,* **46,** 460–475.

Card, P. A., and A. Barcilon, 1982: The Charney stability problem with a lower Ekman layer. *J. Atmos. Sci.,* **39,** 2128–2137.

Cayan, D., 1992: Latent and sensible heat flux anomalies over the northern oceans: Driving the sea surface temperature. *J. Phys. Oceanogr.,* **22,** 859–881.

Cehelsky, P., and K. Tung, 1991: Nonlinear baroclinic adjustment. *J. Atmos. Sci.,* **48,** 1930–1947.

Chen, G., I. Held, and W. Robinson, 2007: Sensitivity of the latitude of the surface westerlies to surface friction. *J. Atmos. Sci.,* **64,** 2899–2915.

da Silva, A., C. Young, and S. Levitus, 1994: *Algorithms and Procedures*. Vol. 1, *Atlas of Surface Marine Data 1994,* NOAA Atlas NESDIS 6, 83 pp.

Delworth, T., and R. Greatbatch, 2000: Multidecadal thermohaline circulation variability driven by atmospheric surface flux forcing. *J. Climate,* **13,** 1481–1495.

Dong, B., and R. Sutton, 2005: Mechanism of interdecadal thermohaline circulation variability in a coupled ocean–atmosphere GCM. *J. Climate,* **18,** 1117–1135.

Ferreira, D., C. Frankignoul, and J. Marshall, 2001: Coupled ocean–atmosphere dynamics in a simple midlatitude climate model. *J. Climate,* **14,** 3704–3723.

Frankignoul, C., 1985: Sea surface temperature anomalies, planetary waves, and air-sea feedback in the middle latitudes. *Rev. Geophys.,* **23,** 357–390.

——, and E. Kestenare, 2002: The surface heat flux feedback. Part I: Estimates from observations in the Atlantic and the North Pacific. *Climate Dyn.,* **19,** 633–647.

——, ——, M. Botzet, A. Carril, H. Drange, A. Pardaens, L. Terray, and R. Sutton, 2004: An intercomparison between the surface heat flux feedback in five coupled models, COADS and the NCEP reanalysis. *Climate Dyn.,* **22,** 373–388.

Gutowski, W. J., 1985: Baroclinic adjustment and the midlatitude temperature profiles. *J. Atmos. Sci.,* **42,** 1735–1745.

——, L. E. Branscome, and D. Stewart, 1989: Mean flow adjustment during life cycles of baroclinic waves. *J. Atmos. Sci.,* **46,** 1724–1737.

Hansen, J., I. Fung, A. Lacis, D. Rind, S. Lebedeff, R. Ruedy, G. Russell, and P. Stone, 1988: Global climate changes as forecast by Goddard Institute for Space Studies three-dimensional model. *J. Geophys. Res.,* **93** (D8), 9341–9364.

Hartmann, D., 1994: *Global Physical Climatology*. Academic Press, 411 pp.

Hsiung, J., 1986: Mean surface energy fluxes over the global ocean. *J. Geophys. Res.,* **91,** 10 585–10 606.

James, I. N., 1987: Suppression of baroclinic instability in horizontally sheared flows. *J. Atmos. Sci.,* **44,** 3710–3720.

——, and L. J. Gray, 1986: Concerning the effect of surface drag on the circulation of a baroclinic planetary atmosphere. *Quart. J. Roy. Meteor. Soc.,* **112,** 1231–1250.

Jin, F.-F., 1997: A theory of interdecadal climate variability of the North Pacific ocean–atmosphere system. *J. Climate,* **10,** 1821–1835.

Kållberg, P., P. Berrisford, B. Hoskins, A. Simmons, S. Uppala, S. Lamy-Thépaut, and R. Hine, 2005: *ERA-40 Atlas*. ERA-40 Project Rep. Series 19, 191 pp. [Available online at http://www.ecmwf.int/research/era/ERA-40_Atlas/docs/index.html.]

Kirk-Davidoff, D., and R. Lindzen, 2000: An energy balance model based on potential vorticity homogenization. *J. Climate,* **13,** 431–448.

Kushnir, Y., and I. Held, 1996: Equilibrium atmospheric response to North Atlantic SST anomalies. *J. Climate,* **9,** 1208–1220.

Lee, D., Z. Liu, and Y. Liu, 2008: Beyond thermal interaction between ocean and atmosphere: On the extratropical climate variability due to the wind-induced SST. *J. Climate,* **21,** 2001–2018.

Lin, S., and R. Pierrehumbert, 1988: Does Ekman friction suppress baroclinic instability? *J. Atmos. Sci.,* **45,** 2920–2933.

Lindzen, R. S., 1993: Baroclinic neutrality and the tropopause. *J. Atmos. Sci.,* **50,** 1148–1151.

Morcrette, J., 1991: Radiation and cloud radiative properties in the European Centre for Medium Range Weather Forecasts forecasting system. *J. Geophys. Res.,* **96** (D5), 9121–9132.

Neelin, J., and W. Weng, 1999: Analytical prototypes for ocean–atmosphere interaction at midlatitudes. Part I: Coupled feedbacks as a sea surface temperature dependent stochastic process. *J. Climate,* **12,** 697–721.

Peixoto, J. P., and A. H. Oort, 1992: *Physics of Climate*. Springer-Verlag, 520 pp.

Peng, S., L. Mysak, H. Ritchie, J. Derome, and B. Dugas, 1995: The differences between early and midwinter atmospheric responses to sea surface temperature anomalies in the northwest Atlantic. *J. Climate,* **8,** 137–157.

Russell, G., J. Miller, and L.-C. Tsang, 1985: Seasonal oceanic heat transports computed from an atmospheric model. *Dyn. Atmos. Oceans,* **9,** 253–271.

Schneider, N., A. Miller, and D. Pierce, 2002: Anatomy of North Pacific decadal variability. *J. Climate,* **15,** 586–605.

Seager, R., Y. Kushnir, N. Naik, M. Cane, and J. Miller, 2001: Wind-driven shifts in the latitude of the Kuroshio–Oyashio Extension and generation of SST anomalies on decadal timescales. *J. Climate,* **14,** 4249–4265.

Solomon, A. B., and P. H. Stone, 2001a: Equilibration in an eddy resolving model with simplified physics. *J. Atmos. Sci.,* **58,** 561–574.

——, and ——, 2001b: The sensitivity of an intermediate model of the midlatitude troposphere's equilibrium to changes in radiative forcing. *J. Atmos. Sci.,* **58,** 2395–2410.

Stone, P. H., 1978: Baroclinic adjustment. *J. Atmos. Sci.,* **35,** 561–571.

——, and B. Nemet, 1996: Baroclinic adjustment: A comparison between theory, observations, and models. *J. Atmos. Sci.,* **53,** 1663–1674.

Stull, R., 1988: *An Introduction to Boundary Layer Meteorology*. Kluwer Academic, 666 pp.

Swanson, K., and R. T. Pierrehumbert, 1997: Lower-tropospheric heat transport in the Pacific storm track. *J. Atmos. Sci.,* **54,** 1533–1543.

Trenberth, K., and J. Caron, 2001: Estimates of meridional atmosphere and ocean heat transports. *J. Climate,* **14,** 3433–3443.

——, and D. Stepaniak, 2003: Covariability of components of poleward atmospheric energy transports on seasonal and interannual timescales. *J. Climate,* **16,** 3691–3705.

Valdes, P. J., and B. Hoskins, 1988: Baroclinic instability of the zonally averaged flow with boundary layer damping. *J. Atmos. Sci.,* **45,** 1584–1593.

Welch, W., and K. Tung, 1998: Nonlinear baroclinic adjustment and wavenumber selection in a simple case. *J. Atmos. Sci.,* **55,** 1285–1302.

Yu, B., G. Boer, F. Zwiers, and W. Merryfield, 2009: Covariability of SST and surface heat fluxes in reanalyses and CMIP3 climate models. *Climate Dyn.,* **36,** 589–605.

Zhang, Y., 2009: Nonlinear equilibration of baroclinic eddies: The role of boundary layer processes and seasonal forcing. Ph.D. thesis, Massachusetts Institute of Technology, 266 pp.

——, and P. Stone, 2010: Baroclinic eddy equilibration under specified seasonal forcing. *J. Atmos. Sci.,* **67,** 2632–2648.

——, ——, and A. Solomon, 2009: The role of boundary layer processes in limiting PV homogenization. *J. Atmos. Sci.,* **66,** 1612–1632.

Zurita, P., and R. Lindzen, 2001: The equilibration of short Charney waves: Implications for potential vorticity homogenization in the extratropical troposphere. *J. Atmos. Sci.,* **58,** 3443–3462.

Zurita-Gotor, P., and R. Lindzen, 2004a: Baroclinic equilibration and the maintenance of the momentum balance. Part I: A barotropic analog. *J. Atmos. Sci.,* **61,** 1469–1482.

——, and ——, 2004b: Baroclinic equilibration and the maintenance of the momentum balance. Part II: 3D results. *J. Atmos. Sci.,* **61,** 1483–1499.